

# Simulation of heterogeneity sections obtained by neutrino radiography

Nozomu Takeuchi

*Earthquake Research Institute, University of Tokyo, Yayoi 1-1-1, Bunkyo-ku, Tokyo 113-0032, Japan*

(Received November 18, 2008; Revised April 22, 2009; Accepted May 1, 2009; Online published February 22, 2010)

Heterogeneity sections potentially observed by neutrino radiography are simulated by using  $S$ -velocity tomography models. All of the velocity heterogeneities in these models are assumed to be of thermal origin, and the velocity anomalies are translated into density anomalies by using the scaling relations obtained from previous laboratory experiments. Assuming the use of the IceCube Neutrino Detector, the density anomalies were integrated along the paths to this detector. Five tomography models were tested, but the obtained sections show common features: paths sampling the CMB region beneath Africa and paths sampling the root of East Antarctica are anomalous. Previous studies suggested that these two regions may be chemically distinct. Approximate order estimations suggest that if these regions have 10% density anomalies, IceCube will detect them in about 300 years.

**Key words:** Earth's interior, seismic tomography, neutrino radiography.

## 1. Introduction

In the past two decades, the resolution and accuracy of seismic tomography models have been greatly improved, and there is now a consensus on the larger-scale patterns of velocity heterogeneities in the mantle (e.g., Romanowicz, 2003). However, because various types of origins (thermal and/or chemical) can explain the observed velocity heterogeneities, it is not possible to ascertain whether heterogeneous regions are buoyant or not. This is one of the most important obstacles to a good understanding of geodynamics.

Although density heterogeneities can be constrained by seismic tomography (e.g., Ishii and Tromp, 1999), the reliability of the obtained models is still controversial (e.g., Resovsky and Ritzwoller, 1999; Romanowicz, 2001). It is therefore important to have independent constraints on the density structure. A highly sensitive neutrino telescope, the IceCube Neutrino Detector (Ahrens *et al.*, 2004; Achterberg *et al.*, 2006), is now under construction at the South Pole. Neutrino radiography (e.g., Volkova and Zatsepin, 1974; Wilson, 1984) using this detector should prove to be one of the most promising tools for producing independent constraints on the density heterogeneities in the Earth.

The idea of neutrino radiography is straightforward. The Earth becomes partly opaque for VHE neutrinos with energy greater than a few TeV. Neutrino radiography can deduce the Earth's density structure from the number of neutrino-induced muon events, which can be collected by a kilometer-scale neutrino telescope, e.g., the IceCube. Several studies have proposed projects to constrain radial density structures with sufficient statistical significance by us-

ing either atmospheric neutrinos (e.g., Gonzalez-Garcia *et al.*, 2008) or extraterrestrial neutrinos (e.g., Kuo *et al.*, 1995). Because seismic density models still have uncertainties even in the radial structures (e.g., Kennett, 1998), such constraints are important.

In contrast, I focus here on the detection of laterally heterogeneous density structures. Although detection might not be very easy, it would be useful to estimate which heterogeneities can potentially be observed and what obstacles there are in detecting them. In this study, I simulate the heterogeneity sections under the assumption that all of the velocity heterogeneities are of thermal origin. If the consistency or inconsistency can be confirmed between observed and simulated sections in the future, constraints could be provided on the chemical structures in the Earth. Although the main focus of this study is to show possibly observable chemical heterogeneities, the detectability of these heterogeneities is also discussed.

## 2. Method

To simulate heterogeneity sections, density structure models are needed. Density structure models are required in some geophysical applications, such as geodynamic modeling (e.g., Hager *et al.*, 1985). In such applications, because of uncertainties in the available density structure models, the density heterogeneities have often been derived by scaling (multiplying some constants as functions of depth) the velocity heterogeneities in tomography models. I have followed this procedure here.

### 2.1 Tomography models used

Although a wide variety of models exist, they can be classified into two main categories: those obtained by using short-period data (hereafter referred to as short-wavelength models) and those obtained using broadband data (referred to as long-wavelength models). The short-wavelength models are generally obtained using travel time data of body

wave phases. Because of the accuracy of phase identification and picking, the initial  $P$  travel times are the most extensively used, and most short-wavelength models are  $P$  models. These models have a strong ability to resolve fine structures and have succeeded in revealing, for example, the fates of subducting slabs (e.g., Fukao *et al.*, 1992; van der Hilst *et al.*, 1997). Although efforts have been made to utilize later phases, the quality and quantity of their travel time data have been poor. As a result, most of the models obtained thus far suffer from strongly inhomogeneous data sampling and are relatively weak in constraining global patterns of velocity heterogeneities.

The long-wavelength models are generally obtained by using higher-quality waveform data. Because of the higher sensitivity of surface waveforms to the  $S$ -velocity structure and the well-isolated later body wave phases in the transverse component of body waveforms, most long-wavelength models are  $S$  models. Secondary data (such as body wave travel times, phase velocity of surface waves, and splitting functions of free oscillation modes) are frequently extracted from the waveforms and are inverted (e.g., Ritsema *et al.*, 1999; Masters *et al.*, 2000; Grand, 2002; Montelli *et al.*, 2004). To fully exploit information included in the waveform data, a waveform inversion (e.g., Mégnin and Romanowicz, 2000; Panning and Romanowicz, 2006; Takeuchi, 2007) or a joint inversion of the secondary data and waveform data (e.g., Gu *et al.*, 2001, 2003) is conducted. These procedures are strong in their ability to resolve the long-wavelength features of global lateral heterogeneities but are relatively weak in their ability to resolve fine structures.

The purpose of this study is to simulate the overall pattern of heterogeneities that can be expected to be observed by the IceCube. I therefore focused on the long-wavelength models. Since the simulated patterns might be biased by uncertainties in the tomography models used, I tested and compared the results of five models: SH18CE (Takeuchi, 2007), SAW24B16 (Mégnin and Romanowicz, 2000), SB4L18 (Masters *et al.*, 2000), S20RTS (Ritsema *et al.*, 1999), and S362D1 (Gu *et al.*, 2001). All are  $S$ -velocity models obtained by using broadband waveform data.

## 2.2 Scaling relations used

There is also a wide range of options in choosing scaling relations. Two types of scaling relations are available: those obtained by laboratory experiments (e.g., Karato, 1993) and those obtained by the inversion of geophysical data (e.g., Forte *et al.*, 1994; Ishii and Tromp, 2001). The former are for heterogeneities caused by the assumed origin (e.g., thermal origin), whereas the latter are for heterogeneities in the actual Earth. Because the purpose of this study is to simulate the expected patterns when all of the heterogeneities in the Earth are assumed to be of thermal origin, I focused on the laboratory experiments.

Although many laboratory experiments have been conducted, the most popular scaling relation is probably that obtained by Karato (1993), which I use here. Because the results by Karato (1993) were given only for depths between 200 and 2800 km, it was necessary to extrapolate. Here, the results in this depth range are first fit by using third-order polynomials of the depth. The obtained optimal

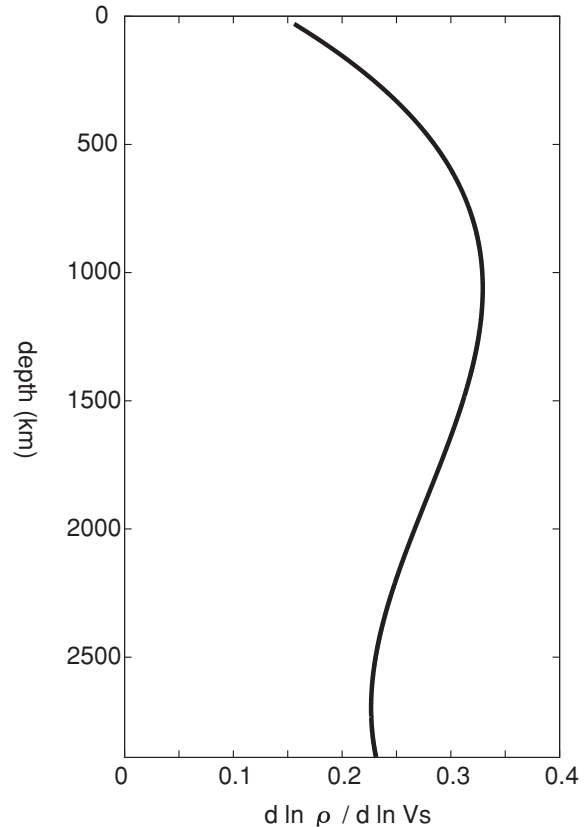


Fig. 1. Scaling relations between the velocity heterogeneities and the density heterogeneities used in this study. The explicit functional form is  $d \ln \rho / d \ln V_s = 0.144 + 4.02 \times 10^{-4} d - 2.64 \times 10^{-7} d^2 + 4.68 \times 10^{-11} d^3$ , where  $d \ln \rho / d \ln V_s$  is a scaling factor and  $d$  is the depth in kilometers.

polynomials (shown in Fig. 1) are then assumed to be the scaling relations for the entire depth of the mantle. Uncertainties do exist due to extrapolating the properties in the normal mantle to boundary layers. However, as long as the (yet unknown) correct scaling factors in these thin layers are in the same order as the assumed values, the overall patterns of heterogeneity sections will not change because we observe the integrated density anomalies along the paths sampling various depths.

## 3. Results

Before I present the simulated results (“integrated cross sections” described later), I will show “central cross sections” revealing the velocity heterogeneity at each central point of a neutrino’s path (Fig. 2). These sections will help us to see which heterogeneity patterns are in the sampling regions. Because the IceCube Neutrino Detector is at the South Pole, all paths are in the north-south direction, and the latitude of the central points depends only on their depth (or the bottoming depth). The latitude of central points is, for example, about  $33^\circ\text{S}$  for paths bottoming at the CMB and about  $76^\circ\text{S}$  for paths bottoming at a 200 km depth.

Figure 3 compares the central cross sections computed for the five different tomography models. We see two distinct features that are commonly observed in the sections. One is the strong low-velocity anomalies in the lowermost mantle at  $0\text{--}45^\circ\text{E}$  (the CMB region beneath Africa). The

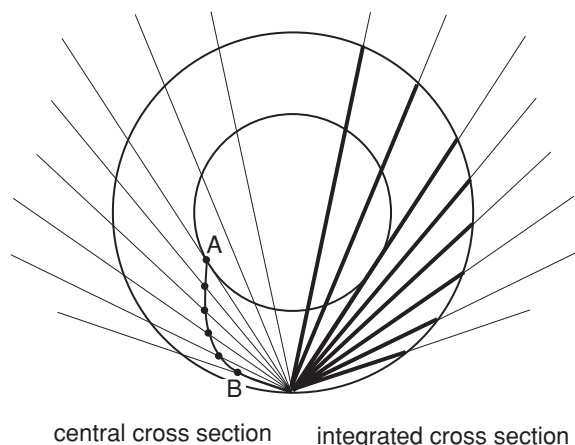


Fig. 2. Two types of cross sections shown in this study. The central cross section is that of the velocity heterogeneities,  $\delta V/V^{(0)}$ , at the central point of the neutrino's path, where  $V^{(0)}$  is the velocity in the standard spherically symmetric model and  $\delta V$  is the velocity perturbation. The integrated cross section is that of the integrated density anomalies along the paths,  $\int \delta \rho dl$ , where  $\delta \rho$  is the density perturbation and  $dl$  is a line segment in the integrated path. Because homogeneity is assumed in the Earth's core, the central cross section is not defined for the central points inside the core, whereas the integrated cross section is defined for all paths. The points A (at the CMB) and B (at the 200 km depth) are located at  $33^\circ\text{S}$  and  $76^\circ\text{S}$ , respectively.

other is the strong high-velocity anomalies in the shallower part of the upper mantle at  $30^\circ\text{W}$ – $140^\circ\text{E}$  (the shallowest 400 km mantle beneath East Antarctica). Both of these anomalies are well-known larger-scale features that are commonly observed in recent tomography models.

The lower-velocity anomalies beneath Africa are suggested even by the early tomography models (e.g., Dziewonski, 1984). Their detailed structures have been studied extensively using regional array data (e.g., Ritsema *et al.*, 1998; Ni *et al.*, 2002, 2005; Ni and Helmberger, 2003). The results suggested that the volume of this anomalous body is large (about 1300 km high, 1200 km across, and 7000 km long), and that the velocity anomalies inside the body are strong (about a 3% velocity reduction throughout this body).

The higher-velocity anomalies beneath East Antarctica are also suggested by the earlier tomography models (e.g., Montagner and Tanimoto, 1991). The feature is independently confirmed by regional analyses (e.g., Ritzwoller *et al.*, 2001; Kobayashi and Zhao, 2004), although the suggested depth extent of this anomalous body is somewhat inconsistent among studies.

In neutrino radiography, we observe the integrated density anomalies along the paths. The effects of heterogeneities at the central points might not be observed because of cancellation by positive and negative anomalies on the path. We therefore show “integrated cross sections” (the integrated density anomalies along the paths; Fig. 2), which are directly related to the observations by the neutrino detector.

Figure 4 compares integrated cross sections. It can be seen that the mantle parts of the obtained sections generally show similar patterns to those in the “central cross sections” (shown in Fig. 3). The results obtained from the five to-

mography models are generally consistent with each other, suggesting that the uncertainties in the tomography models are not so critical as to change the overall features. Among the consistent features, it is especially notable that the paths sampling the two focused regions also show strong anomalies in the integrated cross sections. This is because the anomalies in these regions are so strong and coherent that they are not likely to be masked by the heterogeneities on the other portions of the path. The averaged cross section (upper-left figure of Fig. 4) shows that the effects of the anomalies beneath Africa and East Antarctica extend between about  $30^\circ\text{W}$ – $90^\circ\text{E}$  and  $60^\circ\text{W}$ – $150^\circ\text{E}$ , respectively.

## 4. Discussion

### 4.1 Possibly detectable chemical heterogeneities

In these simulations, I (1) used velocity heterogeneities in tomography models and (2) translated the velocity anomalies into density anomalies. Of course, both of these processes have uncertainties. However, uncertainty in tomography models appears not to change the overall patterns of the simulated sections, as shown in Fig. 4. Therefore, when we observed inconsistency between the observed and simulated patterns in the overall features, it was likely due to uncertainties in the latter procedure.

In this study, I scaled the velocity anomalies to the density anomalies under the assumption that velocity heterogeneities are all of thermal origin. The predominance of thermal origin is often presumed partly due to the similarity between the observed geoid data and the geoid pattern simulated under this assumption (e.g., Hager *et al.*, 1985). However, the existence of chemical heterogeneities is suggested in several regions, including the two regions focused on here.

The low-velocity provinces in the CMB region (beneath Africa and the Pacific) are considered to be chemically distinct. The regions are suggested to have sharp sides (e.g., Ni *et al.*, 2002; To *et al.*, 2005; Takeuchi *et al.*, 2008), which are not likely to be due to purely thermal anomalies. The regions are also suggested to have an anti-correlation between the shear and bulk sound velocity anomalies by both global tomography (e.g., Ishii and Tromp, 1999; Masters *et al.*, 2000) and regional array analyses (e.g., Wang and Wen, 2007); this anti-correlation is also difficult to explain by thermal anomalies. Two popular scenarios for the chemical distinction are the enrichment of iron obtained via interactions with the iron core and the accumulation of piles of dense materials at the bottom of the mantle upwellings. If either of these scenarios occur, we expect higher-density anomalies, which is the opposite of what would be expected from thermal origin.

The high-velocity regions beneath older continents are also considered to be chemically distinct. Almost every older continent appears to have a high-velocity root about 200–400 km thick. These regions are called the continental tectosphere, which is considered to be buoyant compared with the ambient mantle because of the depletion of a basalt-like component (e.g., Jordan, 1975, 1978). The regions are thus considered to have lower-density anomalies; this is also opposite of what would be expected from thermal anomalies.

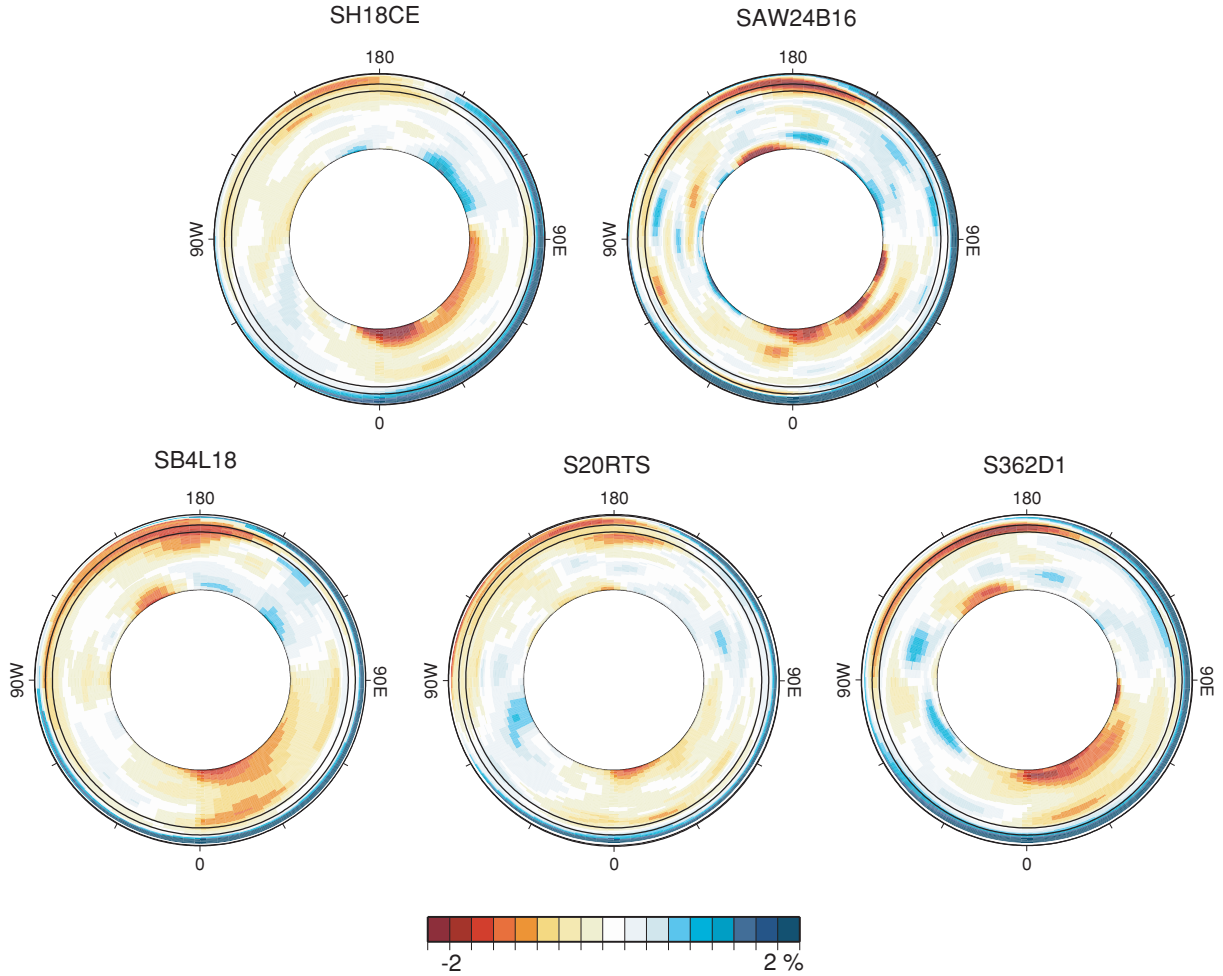


Fig. 3. Comparison of central cross sections for the models SH18CE (Takeuchi, 2007), SAW24B16 (Mégnin and Romanowicz, 2000), SB4L18 (Masters *et al.*, 2000), S20RTS (Ritsema *et al.*, 1999), and S362D1 (Gu *et al.*, 2001). The distance and direction from the center of the figure show the radius and the longitude of the central points, respectively. Downward and upward directions show  $0^\circ\text{E}$  and  $180^\circ\text{E}$ , respectively, and rightward and leftward directions show  $90^\circ\text{E}$  and  $90^\circ\text{W}$ , respectively.

When we assume that all heterogeneities are of thermal origin, we expect the heterogeneity patterns shown in Fig. 4. However, if the two regions of focus are in fact chemically distinct, we should expect anomalies with opposite signs. If we could observe the signs of these integrated density anomalies, we can possibly constrain the chemical heterogeneities in these two regions.

#### 4.2 Detectability of the focused features

I will now estimate how realistic it is to detect the focused chemical heterogeneities. The purpose of the estimation is to see the order of the required amount of data. Rigorous statistical evaluations are beyond the scope of this paper.

Gonzalez-Garcia *et al.* (2008; hereafter referred as GG08) discussed the ability of the IceCube Neutrino Detector to distinguish the realistic radially heterogeneous density profile (the density profile of PREM (Dziewonski and Anderson, 1981);  $\rho_{\text{PREM}}$ ) from the homogeneous Earth density profile ( $\rho_{\text{hom}}$ ). They proposed utilizing the atmospheric neutrinos and considered the problem of observing the following quantity for the various zenith angle,  $\theta$ :

$$R(\cos\theta) = \frac{N_\mu(E_\mu^{\text{fin}} > E_\mu^{\text{fin},\text{min}}, \cos\theta, \rho_{\text{PREM}})}{N_\mu(E_\mu^{\text{fin}} > E_\mu^{\text{fin},\text{min}}, \cos\theta, \rho_{\text{hom}})}, \quad (1)$$

where  $N_\mu$  is the number of atmospheric  $\nu_\mu$ -induced muon events, and  $E_\mu^{\text{fin},\text{min}}$  is an energy threshold. Because the Earth's density structure is expected to be close to that of PREM rather than the homogeneous model, the observed  $R$  is expected to deviate from 1. They defined six angular bins and discussed the case for  $E_\mu^{\text{fin}} = 10$  TeV. They computed the expected  $R$  value and its standard deviation for each angular bin. They concluded that 10 years of observations are sufficient to show statistical significance ( $4.7\sigma$  at the maximum) to reject the reference model (the homogeneous density model).

In this study, I consider the same problem except for discussing the following quantity:

$$R'(\cos\theta) = \frac{N_\mu(E_\mu^{\text{fin}} > E_\mu^{\text{fin},\text{min}}, \cos\theta, \rho_{3\text{D}})}{N_\mu(E_\mu^{\text{fin}} > E_\mu^{\text{fin},\text{min}}, \cos\theta, \rho_{\text{PREM}})}. \quad (2)$$

I test whether we can distinguish the realistic laterally heterogeneous density profile ( $\rho_{3\text{D}}$ ) from the laterally homogeneous density profile ( $\rho_{\text{PREM}}$ ). I consider here the following 3D density model: (1) the low-velocity region beneath Africa has  $+10\%$  density anomalies, (2) the region beneath East Antarctica has  $-10\%$  density anomalies, and

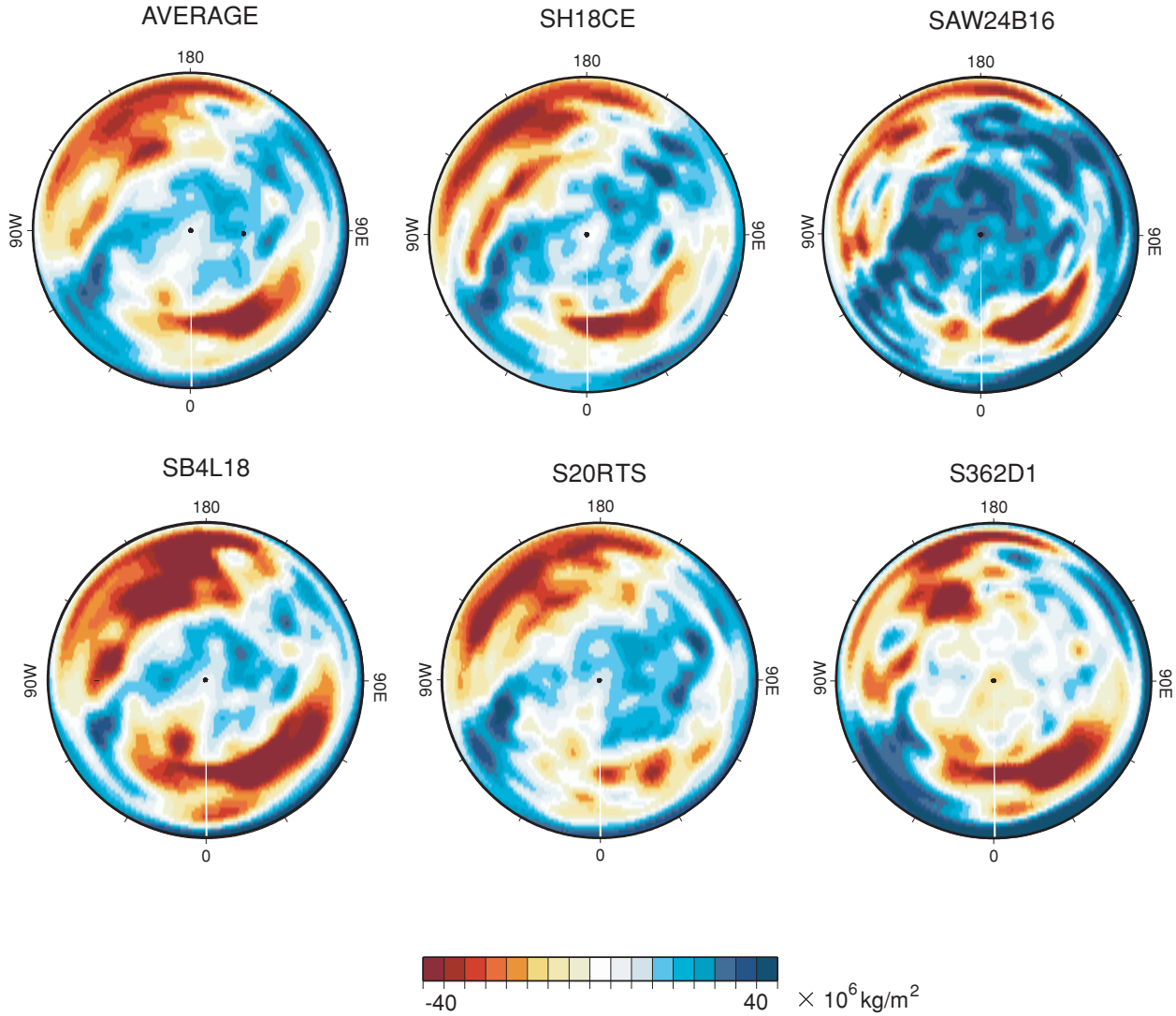


Fig. 4. Comparison of integrated cross sections for the models SH18CE (Takeuchi, 2007), SAW24B16 (Méglin and Romanowicz, 2000), SB4L18 (Masters *et al.*, 2000), S20RTS (Ritsema *et al.*, 1999), and S362D1 (Gu *et al.*, 2001). The average of these five sections (labeled as AVERAGE) is also plotted. The distance and direction from the center of the figure show the radius and the longitude of the central point (or the bottoming point) of each integrated path, respectively. Downward and upward directions show  $0^\circ\text{E}$  and  $180^\circ\text{E}$ , respectively, and rightward and leftward directions show  $90^\circ\text{E}$  and  $90^\circ\text{W}$ , respectively.

(3) the other regions have the density derived from the average over the five velocity models used in Fig. 4. I assume the chemically distinct region beneath Africa as the low-velocity region of the averaged model which is located between depths of 1391 and 2891 (CMB) km,  $50^\circ\text{S}$ – $30^\circ\text{N}$ , and  $30^\circ\text{W}$ – $90^\circ\text{E}$ . I assume the chemically distinct region beneath East Antarctica as the high-velocity region of the averaged model located between depths of 24.4 (Moho) and 400 km,  $60^\circ\text{S}$ – $90^\circ\text{S}$ , and  $60^\circ\text{W}$ – $150^\circ\text{E}$ .

Figures 5(a) and 5(b) show the density length perturbations (difference in the density lengths between the realistic model and the reference model) as a function of the zenith angle for the GG08's problem and the problem in this study, respectively. The perturbations are azimuth dependent for the problem in this study, but I show the averaged perturbations over all azimuths. The perturbations in Fig. 5(a) for  $\cos\theta < -0.83$  are primarily the effects of the density perturbations in the core, while those for  $\cos\theta > -0.83$  are the effects by density perturbations in the mantle. Their

averaged amplitudes are around  $20,000 \times 10^6 \text{ kg/m}^2$  and  $7,000 \times 10^6 \text{ kg/m}^2$ , respectively. The positive perturbations in Fig. 5(b) for  $-0.9 < \cos\theta < -0.7$  and negative perturbations for the other regions are primarily the effects of the anomalies beneath Africa and East Antarctica, respectively. Amplitudes of these anomalies are both about  $200$ – $300 \times 10^6 \text{ kg/m}^2$  on average. These results show that the expected order of the perturbation in this problem is around  $1/100$ – $1/30$  of that in the GG08's problem.

For more quantitative evaluations I approximate Eqs. (1) and (2) as follows:

$$R(\cos\theta) \approx \frac{\exp[-X_{\text{PREM}}(\theta)\sigma_{\text{cc}}(\bar{E}_\nu)]}{\exp[-X_{\text{hom}}(\theta)\sigma_{\text{cc}}(\bar{E}_\nu)]} \quad \text{and} \quad (3)$$

$$R'(\cos\theta) \approx \frac{\exp[-X_{3\text{D}}(\theta)\sigma_{\text{cc}}(\bar{E}_\nu)]}{\exp[-X_{\text{PREM}}(\theta)\sigma_{\text{cc}}(\bar{E}_\nu)]},$$

where  $X_{\text{hom}}$ ,  $X_{\text{PREM}}$ , and  $X_{3\text{D}}$  are the integrated nucleon number density along the neutrino path for the homoge-

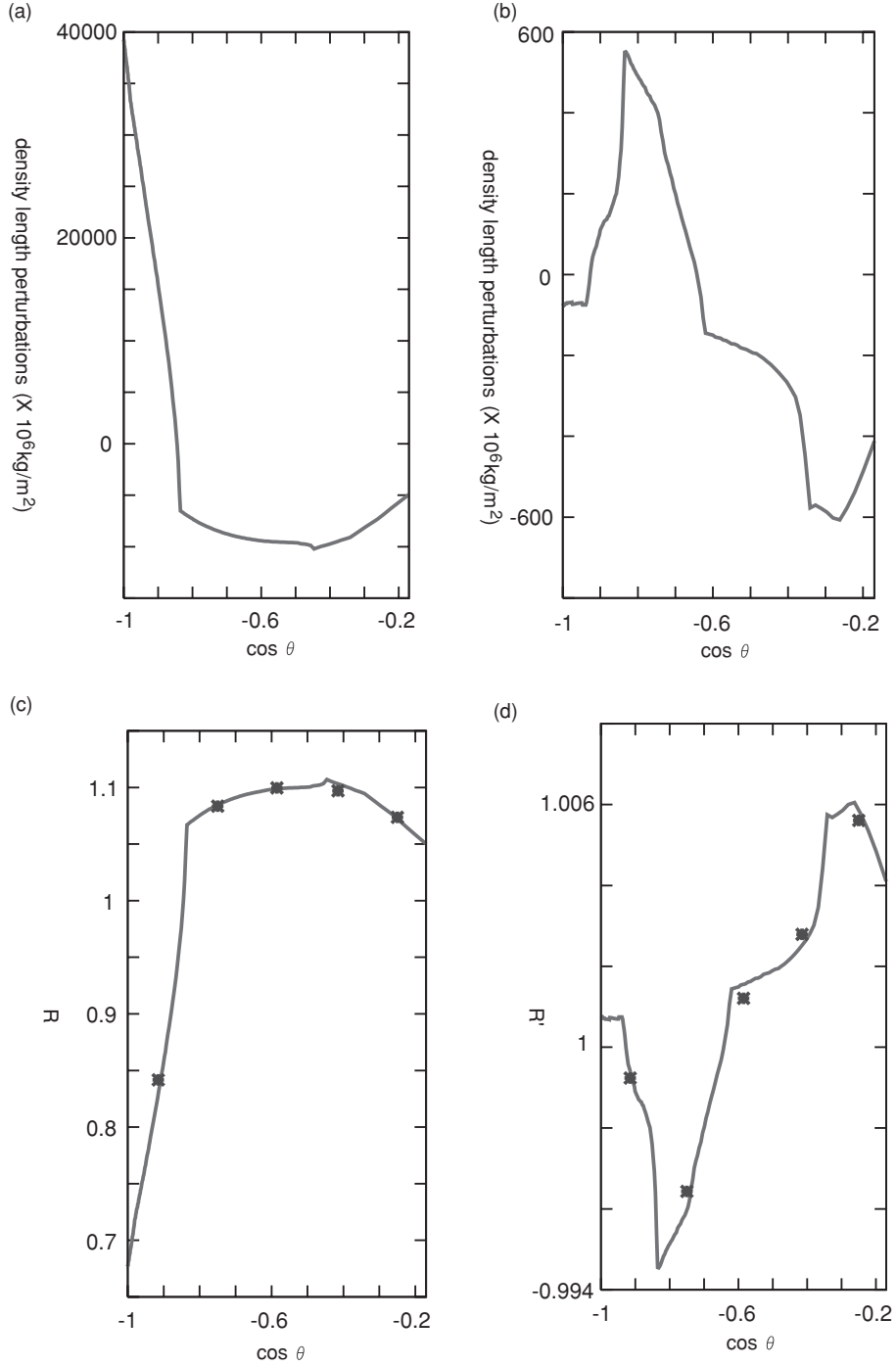


Fig. 5. (a) Density length perturbations for the problem in Gonzalez-Garcia *et al.* (2008) as a function of zenith angles. (b) Density length perturbations for the problem considered in this study. (c)  $R$  values (defined in Eq. (1)) simulated by using Eq. (3). Averaged  $R$  value for each angular bin (denoted by symbols) are also plotted. (d)  $R'$  values (defined in Eq. (2)) simulated by using Eq. (3). Averaged  $R'$  value for each angular bin (denoted by symbols) are also plotted.

neous model, the PREM model, and the 3D model, respectively,  $\sigma_{cc}$  is the neutrino-nucleon scattering cross section, and  $\bar{E}_\nu$  is the representative neutrino energy for the considered energy threshold  $E_\mu^{\text{fin, min}}$ . These equations mean that I approximate that the detected event number  $N_\mu$  is proportional to the detector-side flux of neutrinos with representative energy of  $\bar{E}_\nu$ . I also approximate the statistical errors for the  $i$ -th angular bin,  $\sigma_{\text{stat}, i}$ , to

$$\sigma_{\text{stat}, i} = \sqrt{N_i}/N_i, \quad (4)$$

where  $N_i$  is the number of detected events for the  $i$ -th angular bin. I then define the rejection power for the reference models as

$$\chi^2 = \sum_{i=1}^5 \frac{[R_i - 1]^2}{\sigma_{\text{stat}, i}^2}, \quad \text{and} \quad \chi'^2 = \sum_{i=1}^5 \frac{[R'_i - 1]^2}{\sigma_{\text{stat}, i}^2}. \quad (5)$$

Following the method of GG08, I do not include the events in the most horizontal bin,  $\cos \theta > -0.17$ , to avoid contaminations by backgrounds from possible remaining

misreconstructed downgoing muons. I use the simulated results shown in table 1 in GG08 as  $N_i$  in Eq. (4). I chose here  $\sigma_{cc}(\bar{E}_\nu) = 16.5 \times 10^{-35} \text{ cm}^2$  to reproduce the resultant rejection power  $\chi^2 = 4.7^2$  which was obtained by GG08. Using these assumptions and explicit values, we simulate  $R$  and  $R'$  as a function of a zenith angle (Fig. 5(c) and (d)). Figure 5(c) shows that the results by this approximated method well agree with those by the rigorous method in Gonzalez-Garcia *et al.* (2008; figure 2, center). Figure 5(d) shows that, for the problem in this study, I can expect 0.1–0.5% perturbations in the detected event numbers for each angular bin. The computed rejection power is  $\chi'^2 = 0.19^2$ , which suggests that, to obtain  $1\sigma$  signals, we should improve fivefold in the  $S/N$  ratio. I therefore need about 30 times the amount of data, which suggests that we require about 300 years of observations. Of course, these quantities depend on the amplitudes of the density perturbations assumed in  $\rho_{3D}$ . For example, if we assume 30% density anomalies, the required observation periods will be about 30 years.

**Acknowledgments.** I would like to thank Hiroyuki Tanaka and Hideaki Taira for their valuable comments. Comments by anonymous reviewers were very helpful. This work was supported by Grant-in-Aid for Scientific Research 21740323.

## References

- Achterberg, A., M. Ackermann, J. Adams *et al.*, First year performance of the IceCube neutrino telescope, *Astropart. Phys.*, **26**, 155–173, 2006.
- Ahrens, J., J. N. Bahcall, X. Bai *et al.*, Sensitivity of the IceCube detector to astrophysical sources of high energy muon neutrinos, *Astropart. Phys.*, **20**, 507–532, 2004.
- Dziewonski, A. M., Mapping the lower mantle: determination of lateral heterogeneity in P velocity up to degree and order 6, *J. Geophys. Res.*, **89**, 5929–5952, 1984.
- Dziewonski, A. M. and D. L. Anderson, Preliminary Reference Earth Model, *Phys. Earth Planet. Inter.*, **25**, 297–356, 1981.
- Forte, A. M., R. L. Woodward, and A. M. Dziewonski, Joint inversions of seismic and geodynamic data for models of three-dimensional mantle heterogeneity, *J. Geophys. Res.*, **99**, 21,857–21,877, 1994.
- Fukao, Y., M. Obayashi, H. Inoue, and M. Nenbai, Subducting slabs stagnant in the mantle transition zone, *J. Geophys. Res.*, **97**, 4809–4822, 1992.
- Gonzalez-Garcia, M. C., F. Halzen, M. Maltoni, and H. K. M. Tanaka, Radiography of Earth's core and mantle with atmospheric neutrinos, *Phys. Rev. Lett.*, **100**, 061802, 2008.
- Grand, S. P., Mantle shear-wave tomography and the fate of subducted slabs, *Phil. Trans. R. Soc. Lond. A*, **360**, 2475–2491, 2002.
- Gu, Y. J., A. M. Dziewonski, W.-J. Su, and G. Ekström, Models of the mantle shear velocity and discontinuities in the pattern of lateral heterogeneities, *J. Geophys. Res.*, **106**, 11,169–11,199, 2001.
- Gu, Y. J., A. M. Dziewonski, and G. Ekström, Simultaneous inversion for mantle shear velocity and topography of transition zone discontinuities, *Geophys. J. Int.*, **154**, 559–583, 2003.
- Hager, B. H., R. W. Clayton, M. A. Richards, R. P. Comer, and A. M. Dziewonski, Lower mantle heterogeneity, dynamic topography and the geoid, *Nature*, **313**, 541–545, 1985.
- Ishii, M. and J. Tromp, Normal-mode and free-air gravity constraints on lateral variations in velocity and density of Earth's mantle, *Science*, **285**, 1231–1236, 1999.
- Ishii, M. and J. Tromp, Even-degree lateral variations in the Earth's mantle constrained by free oscillations and the free-air gravity anomaly, *Geophys. J. Int.*, **145**, 77–96, 2001.
- Jordan, T., The continental tectosphere, *Rev. Geophys.*, **13**, 1–12, 1975.
- Jordan, T., Composition and development of the continental tectosphere, *Nature*, **274**, 544–548, 1978.
- Karato, S., Importance of anelasticity in the interpretation of seismic tomography, *Geophys. Res. Lett.*, **20**, 1623–1626, 1993.
- Kennett, B. L. N., On the density distribution within the Earth, *Geophys. J. Int.*, **132**, 374–382, 1998.
- Kobayashi, R. and D. Zhao, Rayleigh-wave group velocity distribution in the Antarctic region, *Phys. Earth Planet. Inter.*, **141**, 167–181, 2004.
- Kuo, C., H. J. Crawford, R. Jeanloz, B. Romanowicz, G. Shapiro, and M. L. Stevenson, Extraterrestrial neutrinos and Earth structure, *Earth Planet. Sci. Lett.*, **133**, 95–103, 1995.
- Masters, G., G. Laske, H. Bolton, and A. Dziewonski, The relative behavior of shear velocity, bulk sound speed, and compressional velocity in the mantle: Implications for chemical and thermal structure, in *Earth's Deep Interior: Mineral Physics and Tomography From the Atomic to the Global Scale*, edited by Karato, S., A. M. Forte, R. C. Liebermann, G. Masters, and L. Stixrude, pp. 63–87, American Geophysical Union, Washington D.C., 2000.
- Mégnin, C. and B. Romanowicz, The three-dimensional shear velocity structure of the mantle from the inversion of body, surface and higher-mode waveforms, *Geophys. J. Int.*, **143**, 709–728, 2000.
- Montagner, J. P. and T. Tanimoto, Global upper mantle tomography of seismic velocities and anisotropies, *J. Geophys. Res.*, **96**, 20,337–20,351, 1991.
- Montelli, R., G. Nolet, F. A. Dahlen, G. Masters, E. R. Engdahl, and S. H. Hung, Finite-frequency tomography reveals a variety of plumes in the mantle, *Science*, **303**, 338–343, 2004.
- Ni, S. and D. V. Helmberger, Ridge-like lower mantle structure beneath South Africa, *J. Geophys. Res.*, **108**, 2094, doi:10.1029/2001JB001545, 2003.
- Ni, S., E. Tan, M. Gurnis, and D. V. Helmberger, Sharp sides to the African superplume, *Science*, **296**, 1850–1852, 2002.
- Ni, S., D. V. Helmberger, and J. Tromp, Three-dimensional structure of the African superplume from waveform modelling, *Geophys. J. Int.*, **161**, 283–294, 2005.
- Panning, M. and B. Romanowicz, A three-dimensional radially anisotropic model of shear velocity in the whole mantle, *Geophys. J. Int.*, **167**, 361–379, 2006.
- Resovsky, J. S. and M. H. Ritzwoller, Regularization uncertainty in density models estimated from normal mode data, *Geophys. Res. Lett.*, **26**, 2319–2322, 1999.
- Ritsema, J., S. Ni, and D. V. Helmberger, Evidence for strong shear velocity reductions and velocity gradients in the lower mantle beneath Africa, *Geophys. Res. Lett.*, **25**, 4245–4248, 1998.
- Ritsema, J., H. J. van Heijst, and H. Woodhouse, Complex shear wave velocity structure imaged beneath Africa and Iceland, *Science*, **286**, 1925–1928, 1999.
- Ritzwoller, M. H., N. M. Shapiro, A. L. Levshin, and G. M. Leahy, Crustal and upper mantle structure beneath Antarctica and surrounding oceans, *J. Geophys. Res.*, **106**, 30645–30670, 2001.
- Romanowicz, B., Can we resolve 3D density heterogeneity in the lower mantle?, *Geophys. Res. Lett.*, **28**, 1107–1110, 2001.
- Romanowicz, B., Global mantle tomography: progress status in the past 10 years, *Ann. Rev. Earth Planet. Sci.*, **31**, 303–328, 2003.
- Takeuchi, N., Whole mantle SH velocity model constrained by waveform inversion based on three-dimensional Born kernels, *Geophys. J. Int.*, **169**, 1153–1163, 2007.
- Takeuchi, N., Y. Morita, N. D. Xuyen, and N. Q. Zung, Extent of the low-velocity region in the lowermost mantle beneath the western Pacific detected by the Vietnamese Broadband Seismograph Array, *Geophys. Res. Lett.*, **35**, L05307, doi:10.1029/2008GL033197, 2008.
- To, A., B. Romanowicz, Y. Capdeville, and N. Takeuchi, 3D effects of sharp boundaries at the borders of the African and Pacific Superplumes: Observation and modeling, *Earth Planet. Sci. Lett.*, **233**, 137–153, 2005.
- van der Hilst, R. D., S. Widiyantoro, and E. R. Engdahl, Evidence of deep mantle circulation from global tomography, *Nature*, **386**, 578–584, 1997.
- Volkova, L. V. and G. T. Zatsepin, *Acad. Sci. U.S.S.R., Bull. Phys. Ser.*, **38**, 151–154, 1974.
- Wang, Y. and L. X. Wen, Geometry and P and S velocity structure of the “African Anomaly”, *J. Geophys. Res.*, **112**, B05313, doi:10.1029/2006JB004483, 2007.
- Wilson, T. L., Neutrino tomography: Tevatron mapping versus the neutrino sky, *Nature*, **309**, 38–42, 1984.